



HAL
open science

Biom mineralization in Barnacle Base Plate in Association with Adhesive Cement Protein

Sunyoung Hur, Christophe Méthivier, Axel Wilson, Michèle Salmain, Souhir Boujday, Ali Miserez

► **To cite this version:**

Sunyoung Hur, Christophe Méthivier, Axel Wilson, Michèle Salmain, Souhir Boujday, et al.. Biom mineralization in Barnacle Base Plate in Association with Adhesive Cement Protein. *ACS Applied Bio Materials*, 2023, 6 (9), pp.3423-3432. 10.1021/acsabm.3c00117. hal-04295451

HAL Id: hal-04295451

<https://hal.science/hal-04295451v1>

Submitted on 17 Nov 2024

HAL is a multi-disciplinary open access archive for the deposit and dissemination of scientific research documents, whether they are published or not. The documents may come from teaching and research institutions in France or abroad, or from public or private research centers.

L'archive ouverte pluridisciplinaire **HAL**, est destinée au dépôt et à la diffusion de documents scientifiques de niveau recherche, publiés ou non, émanant des établissements d'enseignement et de recherche français ou étrangers, des laboratoires publics ou privés.

Hollow Gold Nanoshells for Sensitive 2D Plasmonic Sensors

Daoming Sun^{1,2}, Ferdaous Ben Romdhane³, Axel Wilson¹, Michèle Salmain^{2,*}, Souhir Boujday^{1,*}

¹ Sorbonne Université, CNRS, Laboratoire de Réactivité de Surface (LRS), 4 place Jussieu, F-75005 Paris, France.

² Sorbonne Université, CNRS, Institut Parisien de Chimie Moléculaire (IPCM), 4 place Jussieu F-75005 Paris, France.

³ Sorbonne Université, CNRS, Fédération de Chimie et Matériaux de Paris-Centre (FCMat), Campus Pierre et Marie Curie, 4 Place Jussieu, F-75005 Paris Cedex 05, France.

ABSTRACT

The interaction of incident light with noble metal nanoparticles engenders a fascinating phenomenon known as localized surface plasmon resonance (LSPR). This results in the presence of single or multiple intense absorption bands in the visible to near-infrared spectral range whose position is affected by the refractive index of the surrounding medium. In this comprehensive study, we thoroughly investigated the experimental parameters governing the size, aspect ratio, and optical properties of hollow gold nanoshells (hAuNS) synthesized through galvanic exchange of cobalt-based nanospheres. Subsequently, we rigorously determined both the empirical and theoretical refractive index sensitivity (RIS) and figure of merit (FoM) of these engineered nanostructures. Notably, hAuNS with an external diameter of 98 nm and a shell thickness of 13 nm demonstrated a noteworthy RIS of 360 nm/RIU and a FoM of 2.0 in solution. In contrast, solid gold nanospheres (sAuNS) of a similar diameter exhibited a significantly lower RIS of 136 nm/RIU. Following the transfer of both these nanostructures onto glass slides for the development of LSPR sensors, it was intriguing to note that the RIS and FoM remained largely unaffected. These findings underscore the potential of these plasmonic nanoparticles as promising candidates for the design of sensitive solid-phase LSPR sensing devices.

Keywords:

Hollow Au nanoshells, localized surface plasmon resonance, refractive index sensitivity, figure of merit, surface functionalization, colloids deposition on surfaces.

INTRODUCTION

Noble metal nanoparticles currently undergo extensive developments in biochemical sensing owing to their plasmonic properties.¹⁻⁵ These unique optical features originate from the localized surface plasmon resonance (LSPR), a phenomenon by which conductive band electrons exhibit collective oscillations upon excitation by incident light.⁶ These properties give rise to single or multiple resonance bands^{7,8} in the visible to the near IR spectral region whose position depends on the composition,⁹ shape,¹⁰ and size¹¹ of the plasmonic nanostructures. For a given nanostructure, the position of the LSPR band also depends on the local dielectric environment.¹² As a consequence, changes of the local refractive index (RI) result in measurable shifts of the LSPR band position, which forms the basis of LSPR refractometric sensors.¹³⁻¹⁵ In this line, plasmonic nanoparticles are typically characterized by the so-called refractive index sensitivity (RIS) corresponding to the band shift per RI unit. Another meaningful factor is the figure-of-merit (FoM), defined as the ratio of RIS to full wavelength at half maximum (FWHM). Taking the width of the LSPR band into account is particularly pertinent regarding large nanoparticles, whose RIS tends to be higher, but whose plasmon band is also broadened by multipolar excitations and radiative damping, which makes the band position difficult to define with high accuracy. Both the RIS and the FoM should be maximized in order to improve the analytical performances of LSPR sensors.

One major strategy to enhance the refractometric sensitivity of LSPR sensors is to tune the shape of nanoparticles to optimize their RIS and FoM. In particular, anisotropic nanoparticles such as nanorods,^{16,17} nanocubes,¹⁸ nanoprisms,¹⁹ nanostars,²⁰ nanotriangles²¹ are known to display higher RIS than their spherical counterparts²³.

Nanostructures with sharp features also exhibit strong electromagnetic field enhancement and a higher sensitivity to local RI changes.²⁴

Plasmonic nanoparticles prepared by wet chemistry are usually dispersed in a solvent and stabilized by ligands or surfactants. They can be used as such to design solution-phase optical sensors. However, immobilizing nanostructures on a transparent planar substrate offers practical benefits for LSPR sensing. Among other advantages, it prevents nanoparticles agglomeration, facilitates further functionalization, allows sensor chip regeneration, enables integration within microfluidic systems, and provides portability for commercial use. Unfortunately, immobilization of anisotropic nanoparticles on planar substrates generally induces a decrease of their RIS,^{21,25,26} whose magnitude is directly correlated to the fraction of the nanoparticle surface in contact with the underlying solid support²⁵. As a consequence, gain in RIS brought by anisotropic nanoparticles (e.g., rods, cubes, and plates) with respect to spherical ones is partially lost upon their immobilization.

In contrast, spheres naturally display a low contact area when immobilized on planar surfaces. In this context, hollow Au nanoshells (hAuNS), composed of a solvent-filled core and a metallic gold shell may appear as an attractive alternative to anisotropic nanostructures to build up sensitive LSPR sensors.²⁷ Their core-shell structure affords attractive features such as double interface, spherical shape, and lower gold content. The coupling of external and internal surfaces enhances the plasmonic field²⁸ and provides more contact area with the surrounding medium²⁹. Using a simple model, it was shown that plasmonic coupling between the two surfaces is stronger upon reduction of the shell thickness, making the LSPR band position highly tunable (up to the NIR) and enhancing the RIS.³⁰ Indeed, in a seminal work by Sun and Xia, hollow gold nanoshells were shown to display a 7-fold higher RIS than solid Au nanospheres

(sAuNS) of the same diameter.³¹ A recent single-particle study also demonstrated a remarkable improvement of RIS when solid gold nanospheres (sAuNS) were replaced by hAuNS of similar size.³² Despite their outstanding optical properties, hAuNS have seldom been used to build up refractometric^{33,34} or colorimetric biosensors^{35,36}. To effectively apply hAuNS in substrate-based LSPR sensing, their geometric parameters first ought to be optimized to obtain nanostructures exhibiting both high RIS and FoM. Furthermore, engineering a straightforward LSPR sensor chip utilizing hAuNS is still to be done to demonstrate their superior refractometric sensing properties compared to sAuNS and anisotropic gold nanoparticles.

In a recent work by Zhang et al. a robust and reliable method allowing the synthesis of hAuNS with tunable thickness and diameter was established and the mechanism has been fully characterized. In this study, we build up on this strategy to thoroughly investigate hollow gold nanoshells (hAuNS) produced through galvanic exchange of cobalt-based templates. We engineer and characterize hAuNS with a large range of different diameters (in the range 18 to 106 nm) and shell thicknesses (from 3 to 13 nm) then determine their experimental RIS and FoM. We investigate the influence of the size and thickness on the optical properties of hAuNS to achieve the optimal performances for refractometric biosensors. Discrete dipole approximation (DDA) calculations are also performed to further understand the effect of geometric parameters on their optical properties. In a second part, the potential of the hAuNS nanostructures exhibiting the highest FoM as solid-phase LSPR sensing devices is compared to that of sAuNS of similar size. To that end, both hollow and solid nanostructures are immobilized on chemically functionalized glass slides and the RIS and FoM of the resulting sensor chips are estimated theoretically and experimentally.

EXPERIMENTAL SECTION

Materials. Cobalt chloride hexahydrate ($\text{CoCl}_2 \cdot 6\text{H}_2\text{O}$), trisodium citrate ($\text{Na}_3\text{C}_6\text{H}_5\text{O}_7 \cdot 2\text{H}_2\text{O}$), sodium borohydride (NaBH_4), chloroauric acid trihydrate ($\text{HAuCl}_4 \cdot 3\text{H}_2\text{O}$), sulfuric acid (98%), (3-aminopropyl)triethoxysilane (APTES), toluene, sucrose (99%), hydroquinone (HQ), Tween 20 were bought from Sigma Aldrich. Deionized (DI) water ($18.2 \text{ M}\Omega \text{ cm}$) was collected from a MilliQ device.

Synthesis of hAuNS. Hollow Au nanoshells were synthesized by the previously reported galvanic replacement method³⁷ with slight modifications. Briefly, to produce hAuNS colloids, two stock solutions were prepared: cobalt-based nanoparticle (Co_2B) scaffolds and aqueous HAuCl_4 . For Co_2B , a 100 mL aqueous solution of 0.4 mM $\text{CoCl}_2 \cdot 6\text{H}_2\text{O}$ and 4.0 mM $\text{Na}_3\text{C}_6\text{H}_5\text{O}_7 \cdot 2\text{H}_2\text{O}$ was prepared in a double-neck flask. This solution was bubbled with nitrogen for 1 h to exclude oxygen from the solution and the flask. 1.0 M NaBH_4 aqueous solution was prepared in advance and allowed to fully hydrolyze to $\text{B}(\text{OH})_4^-$. Then, a given volume of 1.0 M $\text{B}(\text{OH})_4^-$ solution (0 – 180 μL) was mixed with 120 μL of freshly prepared 1.0 M NaBH_4 solution and rapidly injected into the deaerated cobalt salt solution under vigorous stirring and nitrogen. After a period of time (ranging from a few seconds to 20 minutes, depending on the amount of $\text{B}(\text{OH})_4^-$), the solution changed from colorless to either brown or grey, indicating the formation of the Co-based NPs. The Co_2B solution was kept for 1 h under nitrogen flow to ensure complete hydrolysis of NaBH_4 . In another flask, a volume of 0.1 M HAuCl_4 (40–160 μL , depending on the targeted thickness) was added to 100 mL of DI water deaerated by nitrogen bubbling for 1 h. Then, 100 mL Co_2B NPs solution was quickly poured into the HAuCl_4 solution under vigorous stirring and nitrogen bubbling. After 5 min, the nitrogen flow was stopped, and the solution was exposed to air under stirring. The remaining cobalt cores were gradually oxidized by oxygen to Co^{2+} and dissolved

in the bulk solution. Once the oxidation was complete, the color of the hAuNS solution changed to pink, purple, blue, or green, depending on the diameter and shell thickness of the nanostructures.

Synthesis of sAuNS. 107-nm solid Au nanospheres were synthesized using the seed-growth method^{38,39} with slight changes. Briefly, Au seeds were prepared by adding 900 μL of 34 mM $\text{Na}_3\text{C}_6\text{H}_5\text{O}_7 \cdot 2\text{H}_2\text{O}$ to 30 mL of 290 μM HAuCl_4 in boiling water. Heating was stopped after 10 min and the solution allowed to cool down to room temperature. Then, 250 μL of 29 mM HAuCl_4 and 200 μL seed solution were added to 100 mL of DI water. The growth of Au seeds was initiated by adding 50 μL of 34 mM trisodium citrate and 250 μL of 0.03 M HQ under vigorous stirring at room temperature. The final solution was kept in the refrigerator until use.

Immobilization of Au nanoparticles on glass surfaces. A microscope cover glass (60×25 mm) was cut into 60×8 mm pieces and extensively washed before functionalization. Glass spectrophotometer cuvettes were used as containers for all the functionalization steps in order to enable the adsorption of Au nanoparticles onto both sides of the glass slides. First, the glass slides were dipped into H_2SO_4 and shaken for 1 h. After washing, glass slides were immersed in a cuvette filled by boiling DI water for 30 min and dried with nitrogen flow. Dry slides were then dipped into cuvettes containing 3.5 mL of APTES solution (0.5 % v/v) in toluene at 90°C for 60 min. After sonication in toluene for 5 min, silanized glass slides were heated to 120°C for 1 h in an oven. Finally, glass slides were cooled to room temperature and immersed in colloidal solutions of sAuNS or hAuNS for 2 h. Upon immobilization of Au nanoparticles, sensor chips were extensively washed with DI water and stored in a dark place.

Measurement of refractive index sensitivity and figure of merit. Extinction spectra were measured using a Cary 50 spectrophotometer (Varian). To adjust the surrounding RI of Au nanoparticles, aqueous solutions containing varying sucrose concentrations (0 to 40 wt%) were used. Colloidal suspensions of hAuNS were centrifuged at 500 to 15000 rcf, according to the particle size. Tween 20 was added to the solid gold nanospheres sAuNS to a final concentration of 0.025 wt% to avoid their aggregation during centrifugation. Then they were centrifuged at 500 rcf and redispersed in DI water to remove excess Tween 20. To adjust the surrounding RI of the gold nanostructures, supernatants were removed and the precipitate redispersed in the sucrose solutions. Alternatively, the sensor chips were immersed in a cuvette filled with sucrose solutions. UV-Vis spectra were recorded and the LSPR band maximum measured. The LSPR band position was plotted against the RI of sucrose solution. Linear regression analysis of the data gave the RIS as the slope of the fit. The FoM is defined as the RIS divided by the FWHM of the plasmon band measured on the extinction spectra.

Electron microscopy. Transmission electron microscopy (TEM) images of the nanoparticles were obtained using a JEOL JEM 1011 microscope operating at an accelerating voltage of 100 kV. Samples were prepared by depositing a drop of particle suspension onto a carbon-coated copper grid and drying the grid at room temperature before imaging. Size distribution, diameter and thickness were established by counting a minimum of 200 particles and 200 shells using Image J software. High resolution transmission electron microscopy (HRTEM) was carried out using a JEOL 2100 Plus UHR microscope operating at 200 kV. Scanning transmission electron microscopy (STEM) images using a high-angle annular dark-field (HAADF) detector were also acquired. The image contrast in this mode is strongly correlated to the atomic number:

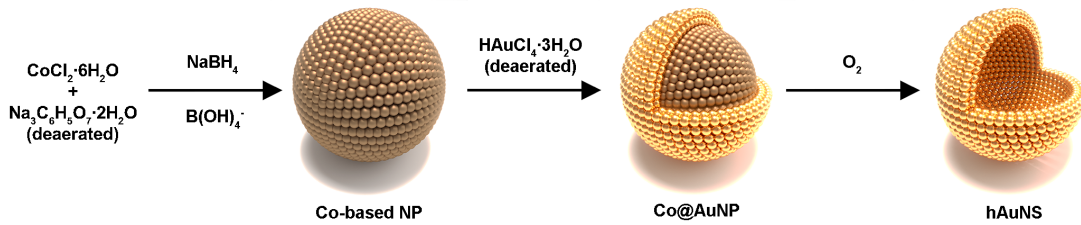
heavier elements contribute to brighter contrast (Z-contrast). Analytic investigations were performed with an energy dispersive X-ray (EDX, Oxford Instruments X-Max 80 SDD) spectrometer attached to the microscope column. Scanning electron microscopy (SEM) imaging was performed with a Hitachi SU-70 FESEM (Field Emission SEM) operating at low accelerating voltages (1 to 5 kV range) and adapted setup in order to overcome the insulating properties of the glass slides and observe the particles without a coating step that may provide biased information.

Simulation of optical properties of hAuNS. DDA calculations were performed by discrete dipole scattering (DDSCAT) 7.3 software.⁴⁰ Simulation for hAuNS samples used the geometric parameters measured from TEM images. The surrounding medium was set to sucrose solutions used experimentally. The dielectric function of gold was referenced in Johnson and Christy's work.⁴¹ For the convenience of calculation, the interior of hAuNS models was set to vacuum. The LSPR band position was plotted as a function of RI. Linear regression analysis of the data gave the RIS as the slope of the fit. The FoM was the RIS divided by the FWHM of the plasmon band taken from the extinction spectra.

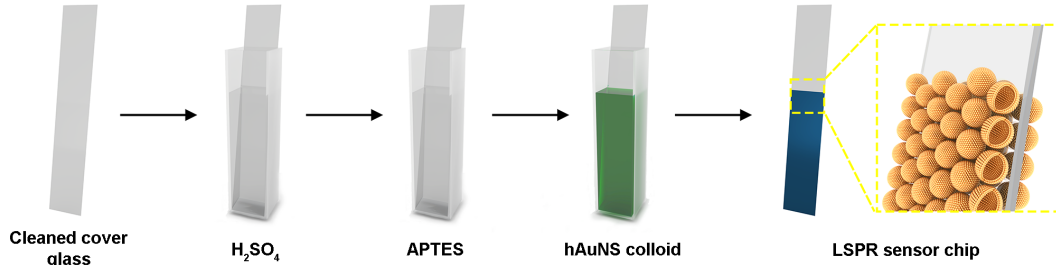
RESULTS AND DISCUSSION

The step-by-step workflow used in the project is depicted in Figure 1. The first part is devoted to the engineering and in-depth characterization of several hollow gold nanostructures (hAuNS) having different geometrical features. Both experimental (UV-Vis and TEM) and theoretical (DDA) investigations are performed. Once the structures exhibiting the best optical responses determined, their transfer to planar surfaces to generate 2D-LSPR sensor chips is investigated and finally the optical responses of the resulting layer thoroughly estimated both theoretically and experimentally.

Synthesis of hAuNS



Fabrication of LSPR sensor chip



Detection of bulk RI change

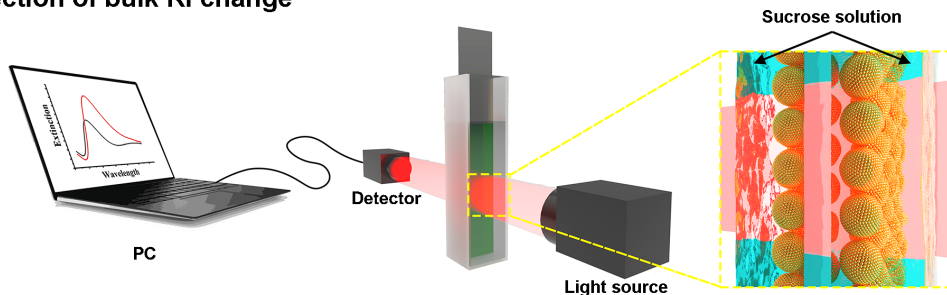


Figure 1: Principle of the bottom-up strategy to prepare substrate-based LSPR sensors and refractometric sensing principle. First, colloidal hAuNS were synthesized through a galvanic replacement reaction using Co₂B nanoparticles as sacrificial templates. Then, dispersed hAuNS were immobilized onto a functionalized glass slide as a simple LSPR sensor chip. At last, the refractive index sensitivity of the sensor chip was determined from the shift of the plasmon band measured with a spectrophotometer

Synthesis and Characterization of hAuNS.

Two important parameters need to be considered for hollow nanostructures, namely the outer diameter and the shell thickness, both correlated to the inner diameter. Herein, hollow nanostructures, hAuNS, were synthesized by galvanic exchange from cobalt-based nanoparticles as sacrificial templates, according to the procedure introduced by Zhang.³⁷ This procedure is based on the synthesis of Co₂B NP intermediates whose size and dispersity can be tightly controlled using B(OH)₄⁻ as growth agent. As depicted in Figure 1, the synthesis of hAuNS consists of three main steps: (1) Co₂B NPs preparation under inert atmosphere by reaction between CoCl₂ and NaBH₄ in the presence of sodium citrate as capping agent and B(OH)₄⁻ (resulting from the complete hydrolysis of NaBH₄) as growth agent to adjust the NP size; (2) Galvanic exchange by addition of HAuCl₄ in anaerobic conditions, during which the Au³⁺ ions are reduced to metallic gold by cobalt to form shells of controlled thickness and rugosity; (3) Oxidation in air and dissolution of the remaining cobalt-based cores to Co²⁺, leaving a cavity of the same size.

Seven hAuNS samples were prepared by varying the amounts of B(OH)₄⁻ and HAuCl₄. To allow for a better visualization of the different hollow Au nanoshells prepared here, a size-to-scale representation of each sample is reported in Figure 2 together with the experimentally measured relevant characteristics of the corresponding hAuNS. In a first set of experiments, the Au-to-Co ratio was kept constant, set to 0.1, and the volume of B(OH)₄⁻ was increased: 0, 60, 120, and 180 μL to progressively increase the size of sacrificial cobalt-based template, the resulting hAuNS are labeled (i), (ii), (iii) and (iv). In the second set of experiments, the volume of B(OH)₄⁻ was kept at 180 μL while the Au-to-Co ratio was increased in the range 0.1, 0.2, 0.3, and 0.4 (hAuNSs labeled (iv), (v), (vi), and (vii)).








Au/Co (at.%)	0.1	0.1	0.1	0.1	0.2	0.3	0.4
1M B(OH) ₄ ⁻ (μL)	0	60	120	180	180	180	180
							
Outer diameter (nm)	18±4	28±5	62±8	83±11	106±15	98±10	82±6
Shell thickness (nm)	3.3±0.7	4.9±1.0	6.6±1.2	7±1	11±2	13±3	12±2
Aspect ratio (d/t)	5.5	5.7	9.5	11.9	9.6	7.5	6.8
LSPR wavelength (nm)	562	609	766	829	818	719	645
FWHM (nm)	190	165	194	284	299	182	156

Figure 2: Summary of synthetic, geometric, and optical parameters of colloidal hAuNS samples. The size-to-scale presentation is drawn according to the average diameter and shell thickness of the corresponding sample measured from TEM images

The extinction spectra and the TEM images of the resulting hAuNS are shown in Figure 3. Additional TEM images are shown in Figure S1 together with size distribution curves. The average outer and inner diameters of the first series, hAuNS (i), (ii), (iii), and (iv), almost linearly increased with the amount of B(OH)₄⁻ (Figure 2 and Figure S2-a). In the absence of B(OH)₄⁻, sample (i), small hAuNS were synthesized (outer diameter 18 nm), while when more B(OH)₄⁻ was used, the average size, inner and outer diameter of hAuNS increased up to 83 nm, demonstrating the role of B(OH)₄⁻ as a growth agent (Figure S2(a)). Moreover, obvious core-shell structures were observed for all the samples on TEM images (Figure 3). The aspect ratio (AR) was calculated as the external diameter-to-shell thickness ratio. These values, shown in Figure 2, increased with B(OH)₄⁻ amount and range from 5.5 to 11.2 from (i) to (iv).

In the second set of experiments, the volume of B(OH)₄⁻ was kept constant at 180 μL while the amount of HAuCl₄ was increased to lead to higher Au-to-Co ratios ranging from 0.1 to 0.4 for samples (iv), (v), (vi) and (vii), vs. 0.1 used in the previous series (Figure 2).

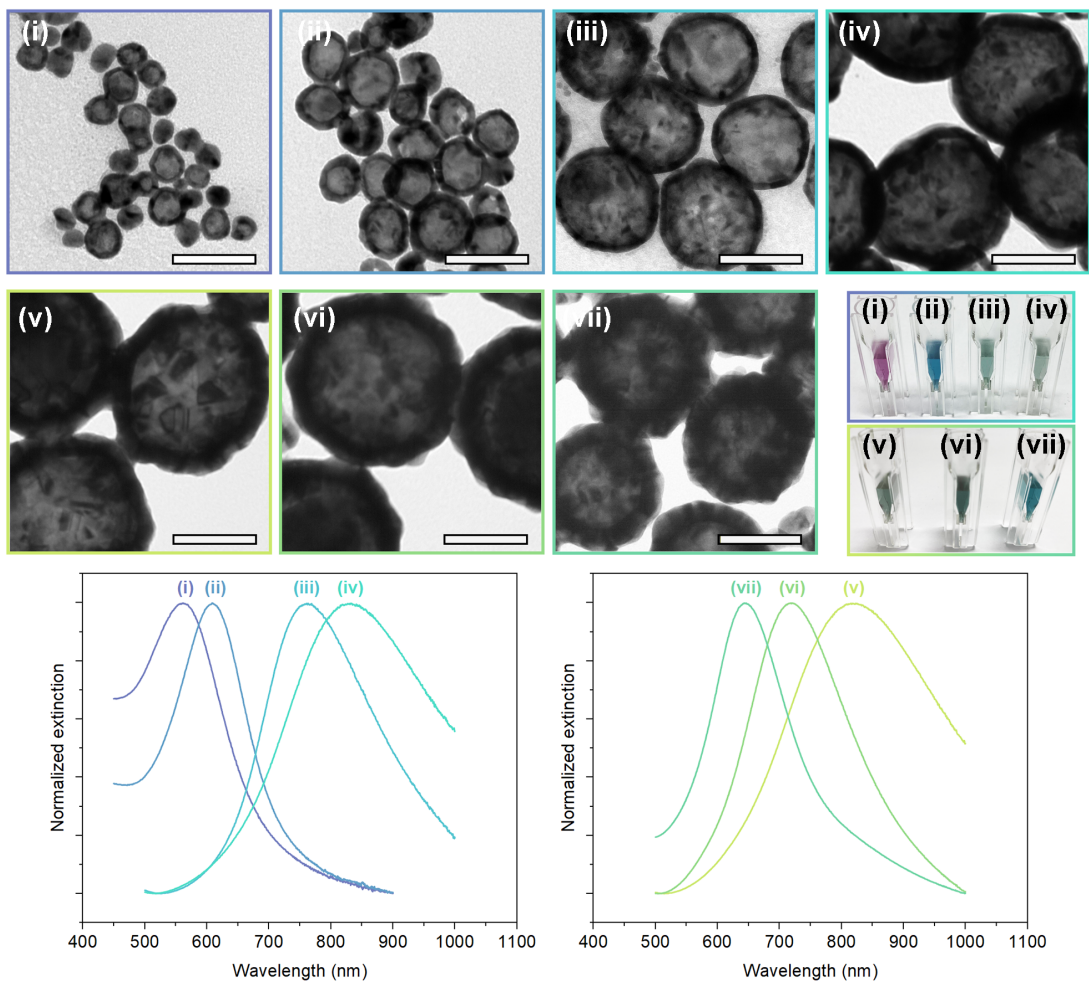


Figure 3: Structural and optical characterization of colloidal hAuNS. TEM images, photos, and extinction spectra of hAuNS (i-vii). The scale bar in all TEM images is 50 nm.

Increasing the Au/Co ratio did not induce dramatic changes in the overall size of the nanoparticles (Figure 2, Figure 3, and Figure S2-b) but led to slightly thicker shells. Consequently, the AR, i.e. the external diameter-to-shell thickness, decreased from 11.2 to 6.7 (Figure 3). However, it is observed that inner and outer diameter and shell thickness changes related to the Au/Co ratio, did not follow any particular trend (Figure S2-b). In addition, the surface of hAuNS with higher Au/Co ratio, i.e. (v), (vi), and (vii), characterized by TEM, appears bumpier than that of previous samples prepared from an Au/Co ratio of 0.1 (see TEM images in Figure 3 and Figure S1). The enlargement of outer diameter and the difference in surface morphology in the presence of high

concentrations of Au^{3+} were also reported in the literature⁴³. The mechanism of galvanic replacement is still not fully understood and difficult to study because of its extremely fast reaction rate. One possible explanation to these differences is that the high concentrations of HAuCl_4 used to synthesize hAuNS (v-vii) possibly lead, during the galvanic exchange, to a substantial amount of Au atoms unevenly nucleated outside the surface of Co-based NP rather than occupying the position of cobalt, thus increasing the outer diameter and roughening the surface of the resulting hAuNS. Consequently, the outer diameter of the hAuNS is determined by both the Au^{3+} concentration and not solely by the size of the Co-based NPs. Notably, 98- and 106-nm diameter hAuNS were prepared using a large amount of HAuCl_4 (Au/Co at% = 20 and 30%, respectively). Of note, these amounts are larger than those previously used by Zhang et al. (Au/Co at% = 3–17%), showing the versatility of this strategy for the synthesis of hAuNS.³⁷

As shown in Figure 3, the hAuNS colloids exhibit pink, blue, or green color depending on their LSPR wavelength. The LSPR band position of samples (i) to (iv) was redshifted from 562 to 829 nm as the diameter increased and the bandwidth progressively increased to 284 nm (Figure 2). For the second series, hAuNS (iv) to (vii), a blueshift in LSPR wavelength was observed from 829 to 645 nm as the Au/Co ratio was increased. Simultaneously, the LSPR bandwidth became progressively narrower, as seen from the FWHM values in Figure 2. For the two series of the samples prepared here, a linear relation between the LSPR band position and AR was established (Figure S2-c) in agreement with previous observations.⁴² Of note, samples (iv) and (vii) having the same diameter but respective AR of 11.2 and 6.7 showed a difference of LSPR band position of 180 nm.

DDA calculations were performed by setting the outer diameter and the shell thickness as the average values measured from TEM images. On the simulated spectra

shown in Figure S3, the position of the LSPR band is only slightly underestimated; less than 7 % for all samples (Table S1). On the contrary, the theoretical FWHM appeared underestimated for all samples especially for the smallest ones where the deviation reaches 48 % (Table S1). This deviation can be explained by the fact that DDA calculations were performed on a single bare nanoparticle without surfactant nor solvent inside the shell. In addition, for samples (iv-vii), “shoulders” were present in their simulated LSPR spectra (Figure S3), but not in the experimental ones. This is probably due to the multipolar mode of large nanoparticles considered by the software.^{44,45}

RIS and FoM of hAuNS. The RIS of the hAuNS was measured in solution from colloidal suspensions of samples (i) – (vii). hAuNS were dispersed in aqueous solutions containing between 0 and 40 wt % sucrose as a simple mean to change the RI of the surrounding medium and relying on the known colloidal stability of plasmonic nanostructures in these media.^{25,46} hAuNS solutions were analyzed by UV-Vis spectroscopy and the position of the LSPR band was plotted versus the RI of the corresponding solvent, as depicted in Figure S4. The RIS was determined from the linear regression of the data. The FoM was then calculated by dividing the RIS by the FWHM. Figure S3 shows the results obtained from DDA calculations performed to determine the theoretical RIS and FoM. The RI of the surrounding medium was the same as the experimental values (1.333 to 1.400) to estimate the theoretical RIS. The summary of the resulting experimental and theoretical data is shown in Figure 4.

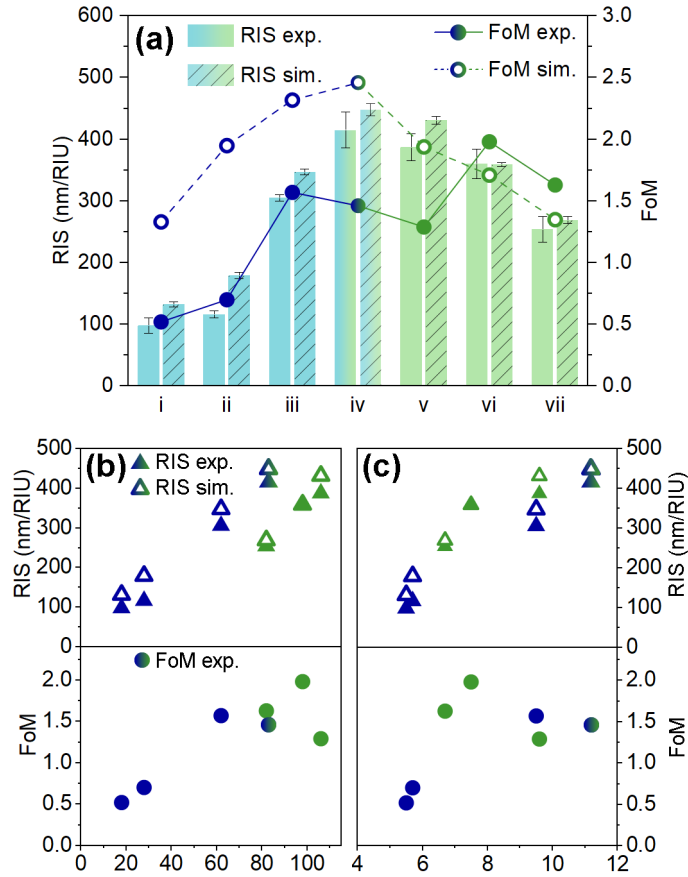


Figure 4: Refractometric sensing properties of colloidal hAuNS samples and their dependency to geometric parameters. (a) Refractive index sensitivity (RIS) and figure-of-merit (FoM) of hAuNS (i-vii). (b) RIS and FoM as a function of outer diameter and (c) RIS and FoM as a function of aspect ratio

For all the nanostructures, the RIS values obtained experimentally are very consistent with the theoretical ones (Figure 4 and Table S2). On the contrary, experimental and simulated FoM values show a noticeable deviation, as expected from the difference in the FWHM discussed above. Nevertheless, the trends of calculated and experimental FoM are consistent (Figure 4-a). In what follows, and due to the discrepancy between experimental and theoretical FWHM, we will not rely on the computational data regarding FoM but rather on the theoretical RIS values.

By increasing the $B(OH)_4^-$ concentration, i.e. the sacrificial template size, the experimental and theoretical RIS of the nanostructures (i-iv) increased from 98 to 415 nm/RIU. hAuNS nanostructures (i) to (iv) show a clear linear correlation between

the RIS and diameter (Figure 4-b). The same correlation is observed when plotting RIS as a function of aspect ratio.

For the second series, nanostructures (iv) to (vi), where the ratio Au/Co was increased, no particular trend nor influence were observed for RIS or FoM, in agreement with the little influence observed regarding the optical properties of these hAuNS. The RIS values for hAuNS (v) – (vi) slightly decreased from 387 to 254 nm/RIU. When the LSPR band of hAuNS is extremely broad, it becomes challenging to determine the band position accurately. For samples (i) – (vii), the FoM ranged from 0.52 to 1.98. The hAuNS (vi) exhibited the highest FoM thanks to its relatively high RIS (360 nm/RIU) and moderate bandwidth (182 nm). Overall, a roughly linear relationship was observed between the RIS and AR, for both series, as shown in Figure 4-c. According to the definition of the AR (d/t) for hAuNS, increasing the diameter and/or reducing the shell thickness results in an increase of the RIS, which is consistent with the literature.^{33,47}

To better visualize the effect of geometric parameters on the optical properties of hAuNS, calculated by DDA, Figure S5 shows the 3D plots and projection maps illustrating the effect of diameter and shell thickness on the LSPR wavelength and the RIS. For modeling convenience, the results are not plotted as function of the aspect ratio, i.e. the external diameter-to-shell thickness ratio, but as function of thickness to outer radius (t/r). Both the LSPR band maximum and the RIS increase exponentially with decreasing shell thickness. This can be attributed to the enhanced plasmonic coupling between the inner and outer surfaces when the distance between them is shortened.^{48,49} At identical aspect ratios, large hAuNS tend to show higher RIS due to the increasing contribution from higher plasmon modes. A threshold is observed for outer diameters of 40–50 nm.

The exponential increase of LSPR band position with reduced shell thickness is also worthy of note. This trend means that the LSPR band position of hAuNS having a thin shell is extremely sensitive to even small variations of shell thickness. As an example, 80-nm diameter hAuNS in a medium of RI = 1.3 shows a LSPR band at 778 nm for $t/r = 0.1$ (AR = 20) or at 680 nm for $t/r = 0.2$ (AR = 10). The band position shifts by 98 nm while the difference in shell thickness is only 4 nm. Experimentally, this could significantly broaden the FWHM of ensemble LSPR bands. It can also explain the large difference in the bandwidth of hAuNS (iv) and (vii) whose average diameters are almost identical.

To sum up and based on the experimental and simulated results aforementioned, hAuNS having a large diameter showed the highest RIS. The extremely broad bandwidth observed at high diameters could be reversed by appropriately increasing the shell thickness. From a synthetic standpoint, optimal conditions were reached by adjusting the amount of HAuCl_4 on the basis of a large Co_2B sacrificial templates. In what follows, the hAuNS (vi) with a 98-nm diameter and 13-nm shell thickness ($\lambda_{\text{max}} = 719$ nm; FWHM = 182 nm) were selected as the optimal nanostructure for the fabrication of LSPR sensor chips.

Before transferring these nanostructures onto planar surfaces, we further performed advanced characterization using HRTEM, STEM-HAADF and EDX

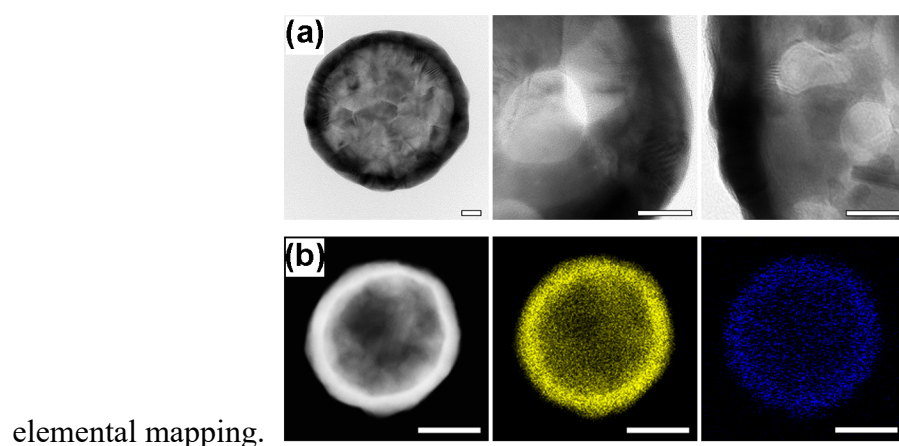


Figure 5 shows HRTEM images and STEM-HAADF image with the corresponding EDX mapping of an individual hAuNS. Additional STEM-HAADF images and STEM-HAADF EDX line scan of an individual hAuNS showing Au and Co content are shown in the SI section (Figure S6) together with STEM-EDX analysis on different hAuNS showing the elemental composition (Table S5).

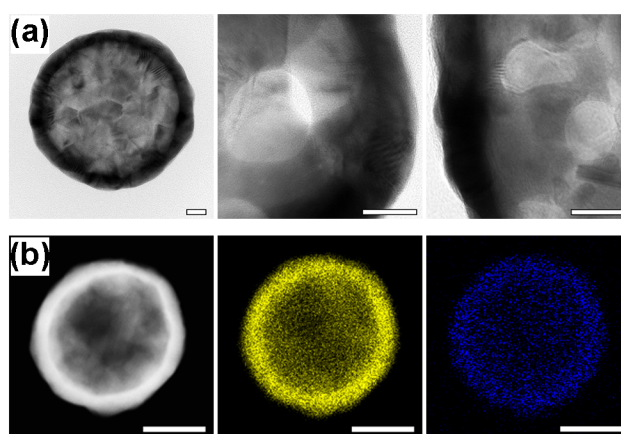
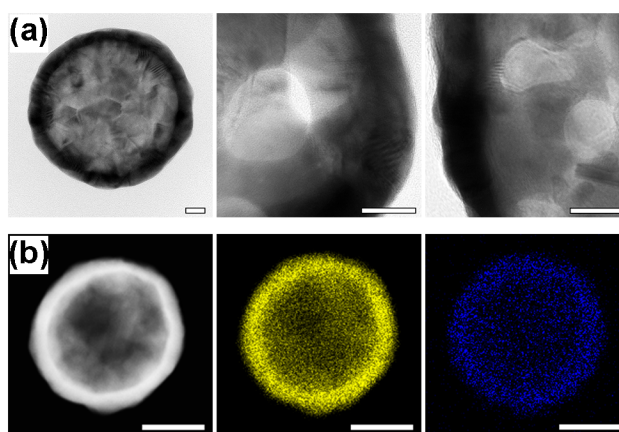


Figure 5: (a) HRTEM images. (b) STEM-HAADF image and corresponding EDX mapping of individual hAuNS. The scale bar is (a) 10 nm and (b) 50 nm.



The HRTEM images in

Figure 5, taken from the edge of an individual hAuNS, clearly highlight the porosity of the nanostructures demonstrating their inner and outer accessibility for sensing applications. This porosity is also clearly visible in HAADF imaging (darker zones) in the SI section (Figure S6), and reveals pores of varying sizes, measuring approximately 10 nm. STEM-EDX analysis were performed to estimate the elemental

composition of the hAuNS. The elemental composition, measured on different points, indicates an atomic composition of Au₉₉Co₁ (Table S5). The starting Au-to-Co ratio was 0.3, which means that, once the Co₂B nanoparticles have fulfilled their mission as sacrificial templates, the cobalt ions are almost entirely removed during the washing steps. This result is different from that previously observed for hollow shells prepared starting from silver sacrificial template, where the silver ions remain trapped within the nanostructures despite extensive rinsing.²⁷ Interestingly, the remaining cobalt is also confined inside the hollow nanosphere as can be seen on the line scan in Figure S6.

LSPR Sensor Chips. Figure 1 illustrates the fabrication of an LSPR sensor chip and detection of RI changes in the surrounding medium. The chip was prepared by immobilizing hAuNS (vi) *via* electrostatic interaction between the negatively charged citrate ligands coating the gold nanostructures and the positively charged homo-condensed network of silanes generated on the glass slides following their functionalization with APTES.⁴³ In parallel, 107-nm diameter solid Au nanospheres (sAuNS) coated by citrate ligands were also synthesized by the seed-growth method and characterized by UV-Vis spectroscopy and TEM (Figure S7). The RIS and FoM of the colloidal suspension of sAuNS was determined following the same procedure as hAuNS. However, we experienced stability issues upon centrifugation of sAuNS and the addition of Tween 20 as an additional capping ligand on top of citrate was necessary to perform these experiments. The resulting RIS and FoM were equal to 136 nm/RIU and 1.0, respectively. The citrate-capped sAuNS were then immobilized on APTES-modified glass slides. The photos, the extinction spectra and the scanning electron microscopy images of the engineered LSPR-sensor chips from hAuNS and sAuNS are

displayed in Figure 6. Figure 6 also shows the RIS and FoM of the chips measured experimentally using sucrose solutions as described above.

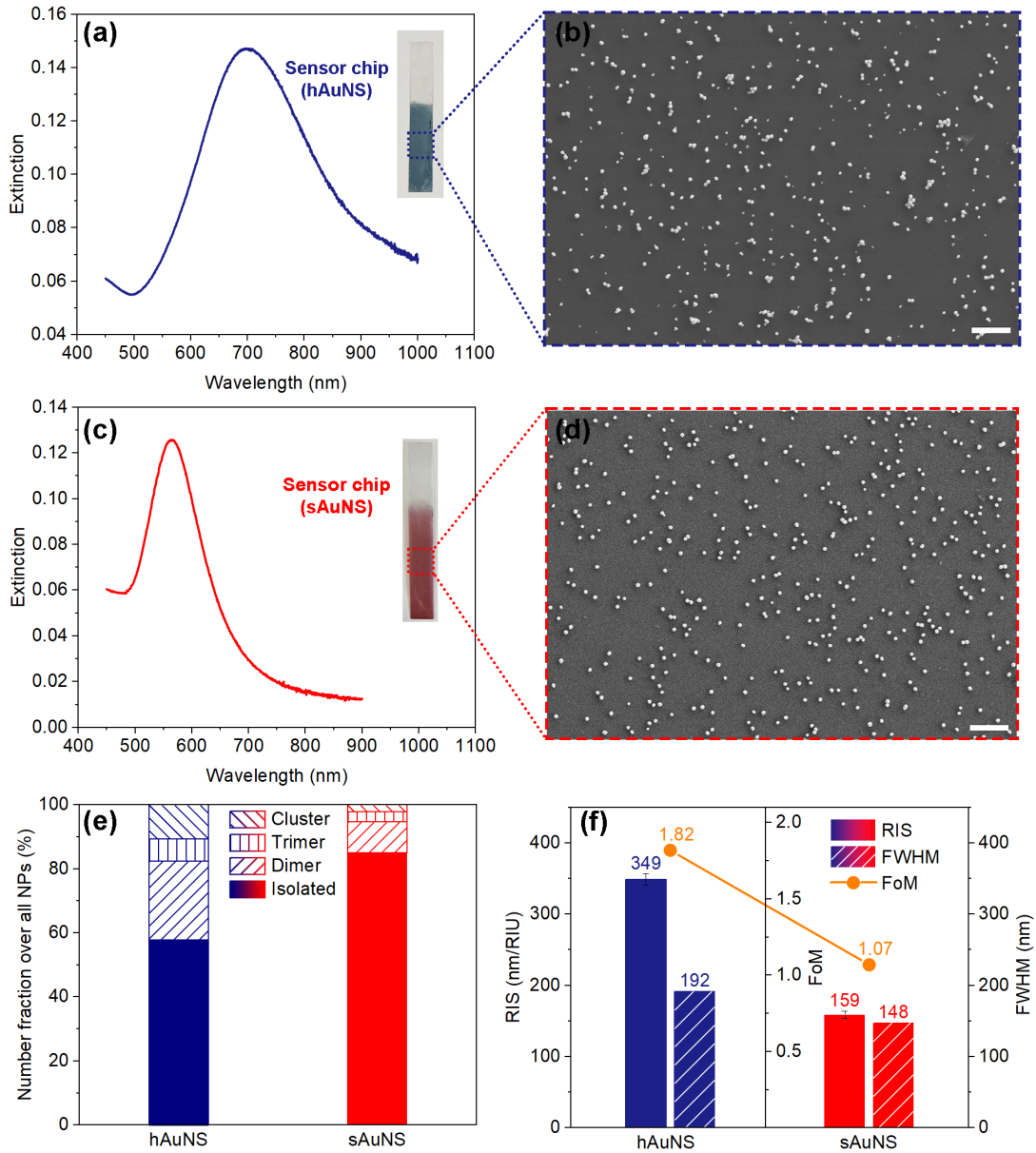


Figure 6: Characterization and refractometric sensing properties of the LSPR sensor chips. Extinction spectra and photos of the sensor chips made of (a) hAuNS and (c) sAuNS immersed in water. SEM images of the immobilized (b) hAuNS and (d) sAuNS on glass slides, scale bar in all SEM images is 1 μ m. (e) Distribution of immobilized nanoparticles on glass slides (f) Comparison of RIS, FWHM, and FoM of hAuNS- and sAuNS-based sensor chips.

The successful immobilization of Au nanostructures at the glass surface was first assessed by visual inspection of the slides that acquired a blue (hAuNS) or a red (sAuNS) hue (insets in Figure 6-a and c). When dipped in pure water, the extinction spectra of both sensor chips displayed a characteristic LSPR band with a maximum at

700 and 564 nm, for hAuNS and sAuNS, respectively. A blue shift of the LSPR band from 719 to 700 and 568 to 564 nm, for hAuNS and sAuNS, respectively, was noticed upon their immobilization on the glass slides. This shift can be attributed to the long-range dipole coupling of large-sized gold nanoparticles.^{50,51} The FWHM of immobilized hAuNS was not affected by the transfer to glass slides, 192 vs. 182 nm (Figure 2 and Figure 6-f), i.e. less than 5 % increase. The same observation is done for sAuNS, an FWHM comparable to the value measured in solution, 148 vs. 133 nm (Figure S7). At the microscopic level, SEM images, shown in Figure 6-b and c, confirm the effective deposition of hAuNS, with the Au nanoparticles randomly distributed, clearly well dispersed on the glass substrate and covering around 3.5 % of the surface area (≈ 5 NPs/ μm^2). Notably, a very small number of clusters could be observed (Figure 6-e), less than 10 % for both hAuNS and sAuNS, demonstrating a homogenous coating in line with the extremely low change noticeable in the FWHM of the LSPR band, and more globally, in the entire extinction spectra. As calculated from the plots in Figure S8, the RIS of the hAuNS sensor chip equaled 349 nm/RIU with a FoM of 1.82 (Figure 6). These values are only slightly lower than those measured for the colloidal suspension (RIS = 360 nm/RIU; FoM = 1.98). The sAuNS sensor chip exhibited a RIS value of 159 nm/RIU with a FoM of 1.07. Surprisingly, the RIS increased upon sAuNS immobilization since it was equal to 136 nm/RIU in solution. The most plausible explanation for this unusual increase in the case of sAuNS, is the interference of the capping ligands, since, as mentioned above, the addition of Tween 20 was necessary to perform RIS measurements in the colloidal solution to prevent nanoparticle aggregation caused by centrifugation. Indeed, the presence of a surfactant layer at the surface of gold nanoparticles was previously shown to reduce the RIS.⁴⁶ On the whole, the refractive index sensitivity and the figure of merit of hAuNS are ca. twice higher than

those of solid counterparts of the same size. We also explored the influence of hAuNS solution concentration on the coverage and optical properties of the resulting sensor chips. The results, in Figures S9 and S10, show that the coverage increases with increasing hAuNSs concentrations but without a significant input to the RIS. For the highest concentration tested, i.e. 5 times the one used in Figure 6, the RIS significantly decreased, possibly due to the excessive blueshift. These findings suggest that the conditions selected here are optimal for a good coverage/RIS balance. Note that, although these experiments were carried out on a different batch of hAuNS, the RIS was highly reproducible for the selected concentration, 347 vs. 349 nm/RIU, evidencing a good reproducibility of the deposition procedure.

To better highlight the potential of these hAuNS in comparison with the existing systems, we gathered in Table S3 the previously published RIS of spherical and anisotropic Au or Ag nanoparticles in solution and once immobilized on a planar substrate.^{21,26} From this table, it appears that, although the RIS of anisotropic nanostructures in solution is higher than that of solid nanospheres, their transfer onto planar surfaces leads to a significant decrease (up to 66 %) thus neutralizing the benefit of using these nanostructures for sensing. Only the spherical nanoparticles exhibit a low decline of RIS because of their minimal contact area with the underlying surface. The hAuNs prepared here have the advantage of the spherical shape but with a considerably higher sensitivity, twice higher than solid spheres. Their transfer to planar surface barely affects their RIS (~3 % decrease) and the resulting sensor chips exhibit the highest sensitivity to date, which makes them ideal systems for the deployment of sensitive 2D plasmonic sensors.

CONCLUSIONS

In this comprehensive study, we thoroughly investigated the experimental parameters influencing the size, aspect ratio, and optical properties of hollow gold nanoshells (hAuNS) produced through galvanic exchange using cobalt-based nanoparticles. We have then experimentally and theoretically determined their refractive index sensitivity (RIS) and figure of merit (FoM) and discussed their correlation to the geometrical features to determine the optimal parameters favorable for LSPR sensing. We found that both the diameter and shell thickness have a significant effect on the RIS; hAuNS with large diameter or thin shell tend to show high RIS. However, in practice, hAuNS with thin shell exhibit a broad LSPR band because of the substantial effect of shell thickness on LSPR band wavelength. The bandwidth can be narrowed by appropriately increasing the shell thickness and thus enhancing the FoM. The RIS and FoM of the optimal hAuNS sample in colloidal solution were found to be 360 nm/RIU and 1.98, respectively, foreshadowing an immense potential as sensing platforms. Notably, upon transfer on planar surface to engineer 2D-LSPR chip, these characteristics were barely modified, less than 3 % decrease in RIS was measured a RIS of 349 nm/RIU and a FoM of 1.82. For comparison, the RIS and FoM of the chip using 107-nm solid sAuNS were 159 nm/RIU and 1.07, respectively. On the one hand, hAuNS show a much higher RIS than their solid counterparts (sAuNS). On the other hand, no obvious decrease in the RIS of hAuNS was observed after they were immobilized on a planar surface. Therefore, this piece of work demonstrates that hAuNS possess distinctive optical characteristics that set them apart from both solid spherical nanoparticles and anisotropic nanoparticles, and make them highly attractive candidates to build up sensitive substrate-based LSPR sensors.

Supporting information:

TEM images, diameter and shell thickness distributions of colloidal hAuNS samples; Experimental and theoretical effect of synthesis parameters on particle size; Extinction spectra and RIS plots of colloidal hAuNS obtained by DDA simulation; Experimental RIS plots of colloidal hAuNS; 3D plots and projection maps illustrating the effect of diameter and shell thickness on the optical properties of hAuNS; STEM-HAADF images and EDX line scan of hAuNS; Characterizations and optical properties of sAuNS; Experimental RIS plots of LSPR sensor chips using hAuNS or sAuNS; Reproducibility experiments for hAuNS-coated glass slides; SEM images of glass slides coated with hAuNS dipped into colloidal hAuNS with varying concentrations; Summary of linear regressions of hAuNS samples determined from DDA simulated and experimental spectra; Experimental and simulated RIS and FoM of hAuNS and sAuNS; STEM-EDX analysis on different hAuNS showing the elemental composition; Summary of changes in RIS for different nanoparticle shapes between dispersed and immobilized states.

Acknowledgements

This work was supported by the Agence Nationale de la Recherche (ANR, project “ChirOptMol”, grant no. ANR-18-CE09-0010). David Montero is gratefully acknowledged for help in conducting SEM experiments. We acknowledge the China Scholarship Council for Ph.D. funding of D. Sun.

Corresponding authors

michele.salmain@sorbonne-universite.fr; souhir.boujday@sorbonne-universite.fr

REFERENCES

- (1) Li, Y.; Schluesener, H. J.; Xu, S. Gold Nanoparticle-Based Biosensors. *Gold Bull.* **2010**, *43* (1), 29–41. <https://doi.org/10.1007/BF03214964>.
- (2) Howes, P. D.; Chandrawati, R.; Stevens, M. M. Colloidal Nanoparticles as Advanced Biological Sensors. *Science* **2014**, *346* (6205), 1247390. <https://doi.org/10.1126/science.1247390>.
- (3) Loiseau, A.; Asila, V.; Boitel-Aullen, G.; Lam, M.; Salmain, M.; Boujday, S. Silver-Based Plasmonic Nanoparticles for and Their Use in Biosensing. *Biosensors* **2019**, *9* (2), 78. <https://doi.org/10.3390/bios9020078>.
- (4) Saha, K.; Agasti, S. S.; Kim, C.; Li, X.; Rotello, V. M. Gold Nanoparticles in Chemical and Biological Sensing. *Chem. Rev.* **2012**, *112* (5), 2739–2779. <https://doi.org/10.1021/cr2001178>.
- (5) Zhao, J.; Zhang, X.; Yonzon, C. R.; Haes, A. J.; Van Duyne, R. P. Localized Surface Plasmon Resonance Biosensors. *Nanomed.* **2006**, *1* (2), 219–228. <https://doi.org/10.2217/17435889.1.2.219>.
- (6) Mayer, K. M.; Hafner, J. H. Localized Surface Plasmon Resonance Sensors. *Chem. Rev.* **2011**, *111* (6), 3828–3857. <https://doi.org/10.1021/cr100313v>.
- (7) Payne, E. K.; Shuford, K. L.; Park, S.; Schatz, G. C.; Mirkin, C. A. Multipole Plasmon Resonances in Gold Nanorods. *J. Phys. Chem. B* **2006**, *110* (5), 2150–2154. <https://doi.org/10.1021/jp056606x>.
- (8) Sonnefraud, Y.; Leen Koh, A.; McComb, D. W.; Maier, S. A. Nanoplasmonics: Engineering and Observation of Localized Plasmon Modes. *Laser Photonics Rev.* **2012**, *6* (3), 277–295. <https://doi.org/10.1002/lpor.201100027>.
- (9) Singh Sekhon, J.; S Verma, S. Refractive Index Sensitivity Analysis of Ag, Au, and Cu Nanoparticles. *Plasmonics* **2011**, *6* (2), 311–317. <https://doi.org/10.1007/s11468-011-9206-7>.
- (10) Mock, J. J.; Barbic, M.; Smith, D. R.; Schultz, D. A.; Schultz, S. Shape Effects in Plasmon Resonance of Individual Colloidal Silver Nanoparticles. *J. Chem. Phys.* **2002**, *116* (15), 6755–6759. <https://doi.org/10.1063/1.1462610>.
- (11) He, Y. Q.; Liu, S. P.; Kong, L.; Liu, Z. F. A Study on the Sizes and Concentrations of Gold Nanoparticles by Spectra of Absorption, Resonance Rayleigh Scattering and Resonance Non-Linear Scattering. *Spectrochim. Acta. A. Mol. Biomol. Spectrosc.* **2005**, *61* (13–14), 2861–2866. <https://doi.org/10.1016/j.saa.2004.10.035>.
- (12) Mock, J. J.; Smith, D. R.; Schultz, S. Local Refractive Index Dependence of Plasmon Resonance Spectra from Individual Nanoparticles. *Nano Lett.* **2003**, *3* (4), 485–491. <https://doi.org/10.1021/nl0340475>.
- (13) Estevez, M.-C.; Otte, M. A.; Sepulveda, B.; Lechuga, L. M. Trends and Challenges of Refractometric Nanoplasmonic Biosensors: A Review. *Anal. Chim. Acta* **2014**, *806*, 55–73. <https://doi.org/10.1016/j.aca.2013.10.048>.
- (14) Sepúlveda, B.; Angelomé, P. C.; Lechuga, L. M.; Liz-Marzán, L. M. LSPR-Based Nanobiosensors. *Nano Today* **2009**, *4* (3), 244–251. <https://doi.org/10.1016/j.nantod.2009.04.001>.
- (15) Zhang, L.; Mazouzi, Y.; Salmain, M.; Liedberg, B.; Boujday, S. Antibody-Gold Nanoparticle Bioconjugates for Biosensors: Synthesis, Characterization and Selected Applications. *Biosens. Bioelectron.* **2020**, *165*, 112370. <https://doi.org/10.1016/j.bios.2020.112370>.
- (16) Feng, L.; Xuan, Z.; Ma, J.; Chen, J.; Cui, D.; Su, C.; Guo, J.; Zhang, Y. Preparation of Gold Nanorods with Different Aspect Ratio and the Optical Response to Solution

- Refractive Index. *J. Exp. Nanosci.* **2015**, *10* (4), 258–267. <https://doi.org/10.1080/17458080.2013.824619>.
- (17) Pellas, V.; Hu, D.; Mazouzi, Y.; Mimoun, Y.; Blanchard, J.; Guibert, C.; Salmain, M.; Boujday, S. Gold Nanorods for LSPR Biosensing: Synthesis, Coating by Silica, and Bioanalytical Applications. *Biosensors* **2020**, *10* (10), 146. <https://doi.org/10.3390/bios10100146>.
- (18) Jeon, H. B.; Tsalu, P. V.; Ha, J. W. Shape Effect on the Refractive Index Sensitivity at Localized Surface Plasmon Resonance Inflection Points of Single Gold Nanocubes with Vertices. *Sci. Rep.* **2019**, *9* (1), 13635. <https://doi.org/10.1038/s41598-019-50032-3>.
- (19) Martinsson, E.; Shahjamali, M. M.; Enander, K.; Boey, F.; Xue, C.; Aili, D.; Liedberg, B. Local Refractive Index Sensing Based on Edge Gold-Coated Silver Nanoprisms. *J. Phys. Chem. C* **2013**, *117* (44), 23148–23154. <https://doi.org/10.1021/jp408187e>.
- (20) Barbosa, S.; Agrawal, A.; Rodríguez-Lorenzo, L.; Pastoriza-Santos, I.; Alvarez-Puebla, R. A.; Kornowski, A.; Weller, H.; Liz-Marzán, L. M. Tuning Size and Sensing Properties in Colloidal Gold Nanostars. *Langmuir* **2010**, *26* (18), 14943–14950. <https://doi.org/10.1021/la102559e>.
- (21) Hegde, H. R.; Chidangil, S.; Sinha, R. K. Refractive Index Sensitivity of Triangular Ag Nanoplates in Solution and on Glass Substrate. *Sens. Actuators Phys.* **2020**, *305*, 111948. <https://doi.org/10.1016/j.sna.2020.111948>.
- (22) Khlebtsov, B. N.; Khanadeyev, V. A.; Ye, J.; Mackowski, D. W.; Borghs, G.; Khlebtsov, N. G. Coupled Plasmon Resonances in Monolayers of Metal Nanoparticles and Nanoshells. *Phys. Rev. B* **2008**, *77* (3), 035440. <https://doi.org/10.1103/PhysRevB.77.035440>.
- (23) Chen, H.; Kou, X.; Yang, Z.; Ni, W.; Wang, J. Shape- and Size-Dependent Refractive Index Sensitivity of Gold Nanoparticles. *Langmuir* **2008**, *24* (10), 5233–5237. <https://doi.org/10.1021/la800305j>.
- (24) Haes, A. J.; Zou, S.; Schatz, G. C.; Van Duyne, R. P. Nanoscale Optical Biosensor: Short Range Distance Dependence of the Localized Surface Plasmon Resonance of Noble Metal Nanoparticles. *J. Phys. Chem. B* **2004**, *108* (22), 6961–6968. <https://doi.org/10.1021/jp036261n>.
- (25) Martinsson, E.; Otte, M. A.; Shahjamali, M. M.; Sepulveda, B.; Aili, D. Substrate Effect on the Refractive Index Sensitivity of Silver Nanoparticles. *J. Phys. Chem. C* **2014**, *118* (42), 24680–24687. <https://doi.org/10.1021/jp5084086>.
- (26) Hegde, H. R.; Chidangil, S.; Sinha, R. K. Refractive Index Sensitivity of Au Nanostructures in Solution and on the Substrate. *J. Mater. Sci. Mater. Electron.* **2022**, *33* (7), 4011–4024. <https://doi.org/10.1007/s10854-021-07593-9>.
- (27) Zhang, L.; Chen, P.; Loiseau, A.; Brouri, D.; Casale, S.; Salmain, M.; Boujday, S.; Liedberg, B. Spatially Controlled Reduction and Growth of Silver in Hollow Gold Nanoshell Particles. *J. Phys. Chem. C* **2019**, *123* (16), 10614–10621. <https://doi.org/10.1021/acs.jpcc.8b11864>.
- (28) Mahmoud, M. A.; Snyder, B.; El-Sayed, M. A. Surface Plasmon Fields and Coupling in the Hollow Gold Nanoparticles and Surface-Enhanced Raman Spectroscopy. Theory and Experiment. *J. Phys. Chem. C* **2010**, *114* (16), 7436–7443. <https://doi.org/10.1021/jp9109018>.
- (29) Shabaninezhad, M.; Ramakrishna, G. Theoretical Investigation of Size, Shape, and Aspect Ratio Effect on the LSPR Sensitivity of Hollow-Gold Nanoshells. *J. Chem. Phys.* **2019**, *150* (14), 144116. <https://doi.org/10.1063/1.5090885>.
- (30) Prodan, E.; Radloff, C.; Halas, N. J.; Nordlander, P. A Hybridization Model for the

- Plasmon Response of Complex Nanostructures. *Science* **2003**, *302* (5644), 419–422. <https://doi.org/10.1126/science.1089171>.
- (31) Sun, Y.; Xia, Y. Increased Sensitivity of Surface Plasmon Resonance of Gold Nanoshells Compared to That of Gold Solid Colloids in Response to Environmental Changes. *Anal. Chem.* **2002**, *74* (20), 5297–5305. <https://doi.org/10.1021/ac0258352>.
- (32) Hong, Y. A.; Ha, J. W. Enhanced Refractive Index Sensitivity of Localized Surface Plasmon Resonance Inflection Points in Single Hollow Gold Nanospheres with Inner Cavity. *Sci. Rep.* **2022**, *12* (1), 6983. <https://doi.org/10.1038/s41598-022-11197-6>.
- (33) Li, S.; Wu, Q.; Ma, P.; Zhang, Y.; Song, D.; Wang, X.; Sun, Y. A Sensitive SPR Biosensor Based on Hollow Gold Nanospheres and Improved Sandwich Assay with PDA-Ag@Fe₃O₄/rGO. *Talanta* **2018**, *180*, 156–161. <https://doi.org/10.1016/j.talanta.2017.12.051>.
- (34) Lee, T.; Kim, G. H.; Kim, S. M.; Hong, K.; Kim, Y.; Park, C.; Sohn, H.; Min, J. Label-Free Localized Surface Plasmon Resonance Biosensor Composed of Multi-Functional DNA 3 Way Junction on Hollow Au Spike-like Nanoparticles (HAuSN) for Avian Influenza Virus Detection. *Colloids Surf. B Biointerfaces* **2019**, *182*, 110341. <https://doi.org/10.1016/j.colsurfb.2019.06.070>.
- (35) Hwang, J.; Lee, S.; Choo, J. Application of a SERS-Based Lateral Flow Immunoassay Strip for the Rapid and Sensitive Detection of Staphylococcal Enterotoxin B. *Nanoscale* **2016**, *8* (22), 11418–11425. <https://doi.org/10.1039/C5NR07243C>.
- (36) Loiseau, A.; Zhang, L.; Hu, D.; Salmain, M.; Mazouzi, Y.; Flack, R.; Liedberg, B.; Boujday, S. Core-Shell Gold/Silver Nanoparticles for Localized Surface Plasmon Resonance-Based Naked-Eye Toxin Biosensing. *ACS Appl. Mater. INTERFACES* **2019**, *11* (50), 46462–46471. <https://doi.org/10.1021/acsami.9b14980>.
- (37) Lindley, S. A.; Cooper, J. K.; Rojas-Andrade, M. D.; Fung, V.; Leahy, C. J.; Chen, S.; Zhang, J. Z. Highly Tunable Hollow Gold Nanospheres: Gaining Size Control and Uniform Galvanic Exchange of Sacrificial Cobalt Boride Scaffolds. *ACS Appl. Mater. Interfaces* **2018**, *10* (15), 12992–13001. <https://doi.org/10.1021/acsami.8b00726>.
- (38) Perrault, S. D.; Chan, W. C. W. Synthesis and Surface Modification of Highly Monodispersed, Spherical Gold Nanoparticles of 50–200 Nm. *J. Am. Chem. Soc.* **2009**, *131* (47), 17042–17043. <https://doi.org/10.1021/ja907069u>.
- (39) Khoury, R. A.; Ranasinghe, J. C.; Dikkumbura, A. S.; Hamal, P.; Kumal, R. R.; Karam, T. E.; Smith, H. T.; Haber, L. H. Monitoring the Seed-Mediated Growth of Gold Nanoparticles Using *in Situ* Second Harmonic Generation and Extinction Spectroscopy. *J. Phys. Chem. C* **2018**, *122* (42), 24400–24406. <https://doi.org/10.1021/acs.jpcc.8b07176>.
- (40) Draine, B. T.; Flatau, P. J. Discrete-Dipole Approximation For Scattering Calculations. *J. Opt. Soc. Am. A* **1994**, *11* (4), 1491. <https://doi.org/10.1364/JOSAA.11.001491>.
- (41) Johnson, P. B.; Christy, R. W. Optical Constants of the Noble Metals. *Phys. Rev. B* **1972**, *6* (12), 4370–4379. <https://doi.org/10.1103/PhysRevB.6.4370>.
- (42) Schwartzberg, A. M.; Olson, T. Y.; Talley, C. E.; Zhang, J. Z. Synthesis, Characterization, and Tunable Optical Properties of Hollow Gold Nanospheres. *J. Phys. Chem. B* **2006**, *110* (40), 19935–19944. <https://doi.org/10.1021/jp062136a>.
- (43) Lindley, S. A.; Zhang, J. Z. Bumpy Hollow Gold Nanospheres for Theranostic Applications: Effect of Surface Morphology on Photothermal Conversion Efficiency. *ACS Appl. Nano Mater.* **2019**, *2* (2), 1072–1081. <https://doi.org/10.1021/acsanm.8b02331>.
- (44) Wheeler, D. A.; Newhouse, R. J.; Wang, H.; Zou, S.; Zhang, J. Z. Optical

- Properties and Persistent Spectral Hole Burning of Near Infrared-Absorbing Hollow Gold Nanospheres. *J. Phys. Chem. C* **2010**, *114* (42), 18126–18133. <https://doi.org/10.1021/jp1076824>.
- (45) Pu, Y.; Song, F.; Zhang, W.; Lindley, S.; Adams, S.; Zhang, J. Z. Size-Tunable Synthesis of Hollow Gold Nanospheres through Control of Reaction Temperature. *Part. Part. Syst. Charact.* **2017**, *34* (8), 1600255. <https://doi.org/10.1002/ppsc.201600255>.
- (46) Martinsson, E.; Shahjamali, M. M.; Large, N.; Zaraee, N.; Zhou, Y.; Schatz, G. C.; Mirkin, C. A.; Aili, D. Influence of Surfactant Bilayers on the Refractive Index Sensitivity and Catalytic Properties of Anisotropic Gold Nanoparticles. *Small* **2016**, *12* (3), 330–342. <https://doi.org/10.1002/sml.201502449>.
- (47) Tuersun, P. Optimizing the Figure of Merit of Gold Nanoshell-Based Refractive Index Sensing. *Optik* **2016**, *127* (1), 250–253. <https://doi.org/10.1016/j.ijleo.2015.10.069>.
- (48) Jain, P. K.; El-Sayed, M. A. Universal Scaling of Plasmon Coupling in Metal Nanostructures: Extension from Particle Pairs to Nanoshells. *Nano Lett.* **2007**, *7* (9), 2854–2858. <https://doi.org/10.1021/nl071496m>.
- (49) Jain, P. K.; El-Sayed, M. A. Surface Plasmon Resonance Sensitivity of Metal Nanostructures: Physical Basis and Universal Scaling in Metal Nanoshells. *J. Phys. Chem. C* **2007**, *111* (47), 17451–17454. <https://doi.org/10.1021/jp0773177>.
- (50) Nath, N.; Chilkoti, A. Label-Free Biosensing by Surface Plasmon Resonance of Nanoparticles on Glass: Optimization of Nanoparticle Size. *Anal. Chem.* **2004**, *76* (18), 5370–5378. <https://doi.org/10.1021/ac049741z>.
- (51) Jenkins, J. A.; Zhou, Y.; Thota, S.; Tian, X.; Zhao, X.; Zou, S.; Zhao, J. Blue-Shifted Narrow Localized Surface Plasmon Resonance from Dipole Coupling in Gold Nanoparticle Random Arrays. *J. Phys. Chem. C* **2014**, *118* (45), 26276–26283. <https://doi.org/10.1021/jp508181g>.